Available online at www.sciencedirect.com
SCIENCE DIRECT®
International Journal of Heat and Mass Transfer 47 (2004) 1925–1935
International Journal of HEAT and MASS TRANSFER
www.elsevier.com/locate/ijhmt

Control and effect of dissolved air in water during flow boiling in microchannels

Mark E. Steinke, Satish G. Kandlikar *

Thermal Analysis and Microfluidics Laboratory, Department of Mechanical Engineering, Kate Gleason College of Engineering, Rochester Institute of Technology, 76 Lomb Memorial Dr., Rochester, NY 14623, USA

Received 18 April 2003; received in revised form 24 September 2003

Abstract

An experimental investigation is performed to study the control of dissolved gases and their effect on heat transfer and pressure drop during the flow of water in a microchannel. An apparatus is developed to deliver water with different levels of dissolved air for use in heat transfer experiments. Six parallel microchannels, each having a hydraulic diameter of 207 μm, are fabricated in copper. During the flow boiling studies with water in these microchannels, nucleation was observed at a surface temperature of 90.5 °C for the dissolved oxygen content of 8.0 parts per million (ppm) at a pressure of 1 atm with untreated de-ionized water. For the dissolved oxygen contents of 5.4 and 1.8 ppm, nucleation is not observed until the surface temperature reached 100 °C at a pressure of 1 atm. A slight reduction in heat transfer is noted as the bubbles begin to nucleate in the 8.0 ppm case due to the formation of an insulating bubble layer on the heater surface. Previous investigators for flow boiling in large diameter channels did not observe such behavior. Further downstream, the heat transfer is observed to increase due to bubble activity. This result is in agreement with previous studies.

Keywords: Microchannel; Dissolved gas; Flow boiling

1. Introduction

Dissolved gases are present in water at different levels depending on the temperature, solubility, and exposure history. The presence of dissolved gases can serve to enhance or hinder a process. It is important to realize that their presence could impact the heat transfer and pressure drop behavior. This effect should be carefully monitored while generating heat transfer data for pure water.

The amount or solubility of a gas in a fluid can be determined using thermodynamic and ideal gas laws. In addition, Raoult's law provides a simple method to determine the concentration of a species dissolved in a liquid. The law relates the activity of the fluid to the partial pressures. The activity can be assumed to be one when the activity of the components are very close to each other, such as air and water mixtures. If the temperature in the system is above any of the mixture components' critical temperatures an expression using Henry's law is valid. In the most general form, Henry's law expresses the equilibrium amount of dissolved gas in a liquid at a given temperature as follows.

$$C_A = H * P_A \tag{1}$$

where C_A is the mole fraction of the dissolved gas in the liquid, H is the Henry's law constant specific for each gas and temperature dependent, and P_A is the partial pressure of the dissolved gas at equilibrium above the liquid. There are several different values for Henry's law constants, depending upon the reference used. The availability of these different measures of dissolved gas concentration has caused some difficulty in comparing available literature.

* Corresponding author. Tel.: +1-585-475-6728; fax: +1-585-475-7710.
E-mail address: sgkeme@rit.edu (S.G. Kandlikar).

0017-9310/$ - see front matter © 2003 Elsevier Ltd. All rights reserved.
doi:10.1016/j.ijheatmasstransfer.2003.09.031

Nomenclature

A	area (m^2)
C	concentration (ppm)
d	channel depth (m)
D_h	hydraulic diameter (m)
f	friction factor
G	mass flux ($kg/m^2\,s$)
h	heat transfer coefficient ($W/m^2\,K$)
$\bar{h}$	average heat transfer coefficient ($W/m^2\,K$)
H	Henry's law constant
k	thermal conductivity (W/m K)
l	length (m)
$\dot{m}$	mass flow rate (kg/s)
Nu	Nusselt number ($= hD_h/k_f$)
$\overline{Nu}$	average Nusselt number
P	pressure (kPa)
q	heat transfer (W)
q''	heat flux (W/m^2)
Re	Reynolds number ($= G * D_h/\mu$)
T	temperature (°C)
V	volume (m^3)
w	channel width (m)
x	vapor mass fraction at outlet

Greek symbols

α	Bunsen coefficient (ml/100 ml solvent)
α^*	aspect ratio parameter used in fRe calc ($= d/w$)
Δ	difference
ΔT_{LMTD}	log mean temperature difference (°C)
μ	viscosity ($N\,s/m^2$)
ρ	density (kg/m^3)

Subscripts

A	species A
avg	average
cp	constant property
eff	effective
f	fluid
g	gas
H	heat flux
m	mean
s	surface
sat	saturation
T	temperature
TS	test section
w	wall

However, there is one attractive method used in chemistry and is presented in [1]. The use of the Bunsen absorption coefficient α can simplify and provide a comparable measure of dissolved gases. The coefficient, shown in Eq. (2), is a volume fraction with respect to standard temperature and pressure (STP) and partial pressure.

$$\alpha = \frac{V_{gas}(STP)}{V_{solvent}(STP)} * \frac{1}{P_A} \tag{2}$$

where $V_{gas}(STP)$ is the volume of the dissolved gas of interest at STP, $V_{solvent}$ is the volume of the solvent at STP, and P_A is the partial pressure of the solvent. Both the volume of the gas of interest and the volume of the solvent are reduced to volumes at STP. This fraction is then multiplied by the reciprocal of the partial pressure of the dissolved gas of interest. Therefore, the concentration of the gas of interest can be determined knowing the partial pressure of the gas and the volume of the solvent.

The Bunsen absorption coefficient for several gases of interest in water is shown in Fig. 1 [1]. It can be seen that the Bunsen absorption coefficient of air in water reaches an asymptote around 80 °C and is nearly constant approaching saturation temperature at 1 atm. Therefore with a fixed volume of solvent (water), the amount of dissolved air is directly dependent upon the partial pressure of air.

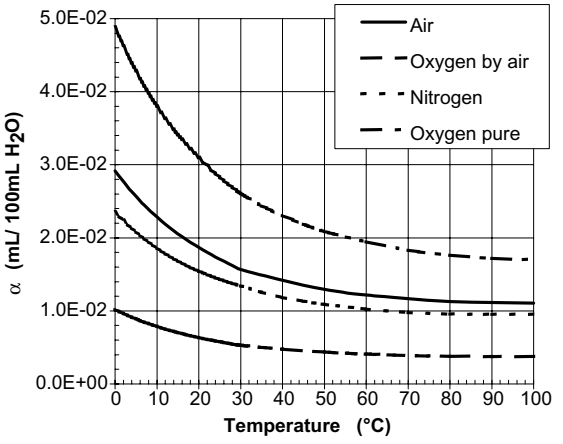

Fig. 1. Bunsen absorption coefficient of dissolved gases of interest in water.

The amount of a gas dissolved in the liquid is proportional to the partial pressure of the gas. To determine the amount of oxygen dissolved in water, the partial pressure of oxygen in air is needed. The mole fraction of oxygen in air is 0.21. Using Eq. (2), the resulting concentration of oxygen dissolved in water at 1 atm is 8.52 mg of oxygen per mg of water, or parts per million (ppm). However, the percentage of oxygen in the dis-

solved air is approximately 34% by volume and varies according to temperature as seen in [1].

In measuring the dissolved gas concentrations, it is very difficult to manufacture an ion selective electrode that measures air concentration. Therefore, an ion selective electrode that measures the concentration of oxygen is generally used to determine the amount of dissolved oxygen in the water. The present work will report the dissolved air content in terms of the dissolved oxygen content in the water.

The solubility of air decreases with an increase in water temperature. This behavior results in gas desorption as the water is heated. Natural cavities present on the heater surface act as nucleation sites for the gas bubbles to form and grow, evaporating some of the water as well. Apparent nucleate boiling is thus initiated at temperatures lower than the saturation temperature of the pure water. The desorption of dissolved gases appears to be similar to the onset of nucleate boiling in subcooled water flow.

There are several experimental and analytical papers investigating the effect of dissolved gases upon heat transfer characteristics. Several of these papers along with some important details are presented in Table 1. The majority of papers studied pool boiling and only seven papers present experimental studies for flow boiling. All of the researchers reported that an increase in the dissolved gas content enhances the heat transfer performance. In addition, several researchers reported that the superheat or the boiling incipience temperature is reduced with an increase in dissolved gas concentration.

Behar et al. [2] experimentally studied the effect of dissolved air in water in a tube. They indicate that the heat transfer improves with dissolved gas content due to the nucleation phenomena. The increase in heat transfer continues well into saturated boiling. At high heat fluxes under fully developed pool boiling conditions, the influence of dissolved gases diminishes and the two curves for pure and gassy cases merge. The effect is very prominent for organic liquids, which can dissolve up to ten times more air than in water. Another interesting fact noted by Behar et al. [2] was that the pressure drop did not increase in forced convection until the beginning of the vaporization region, when the wall temperature reached T_{sat}. This means the heat transfer enhancement could be achieved without a pressure drop penalty as far as the wall temperature was below the saturation temperature of water corresponding to the total system pressure.

An exhaustive study of dissolved gas effects on subcooled flow boiling of fluorocarbons in a 12.7 mm tube was presented by Murphy and Bergles [4]. They presented equations for predicting the onset of nucleation by considering the partial pressure of the dissolved gases. At higher heat fluxes, they noted that the difference between the gassy and degassed liquids diminished and the two boiling curves merged.

Muller-Steinhagen et al. [6] conducted a detailed experimental study on the effect of various gases on water and heptane in a 14.7 mm annulus gap. Their results were similar to those obtained by earlier investigators. They noted that the effect of dissolved gases was relatively small in water.

Chao et al. [7] experimentally studied the effect of air and water in two channels with a hydraulic diameter of 3.9 and 6.3 mm. They report that the heat transfer enhancement following nucleation was as high as 15–20%. Adams et al. [12] experimentally studied the effect of dissolved gases on the flow of water in a channel with a hydraulic diameter of 0.76 mm. They noted an increase in the heat transfer rate due to early gas bubble nucleation. In addition, they reported a dependence of heat transfer coefficient enhancement upon the fluid velocity.

The presence of dissolved gases enhances the heat transfer over a pure fluid case in both pool and flow boiling. However, there is still a need to investigate the effect of dissolved gases over a wider range of mass fluxes, heat fluxes, and channel sizes. The smallest channel size reported in Table 1 is 0.76 mm. This size would be considered as a minichannel under the classifications presented by Kandlikar and Grande [20]. In their classification, a microchannel has a diameter less than 200 μm. There are presently no studies available for the dissolved gas effect on flow boiling in microchannels. The present work is performed to begin to provide experimental data for dissolved gas effect upon flow boiling in microchannels.

2. Objectives of the present work

The present work focuses on developing a technique to generate water with the desired level of dissolved air content. In addition, another goal is determining the effect of the dissolved gas on nucleation characteristics, heat transfer and pressure drop during flow boiling in microchannels.

3. Experimental setup

The experimental setup for the flow loop is designed to deliver a constant mass flow rate of water to a horizontal microchannel test section. The water system delivers de-ionized water with different levels of dissolved air content. Fig. 2 shows the schematic of the water delivery system that includes a pressure chamber, flat plate heat exchanger, throttling needle valve, flow meter, test section, and a condensate collection container. Two different methods are used to pressurize the chambers. The first method is for the gas-saturated case

Table 1
Previous works involving dissolved gas experiments

Author, year	Type/setup	Fluids	C (ppm)[a]	P_{total} (atm)	q'' (kW m^{-2})	G (kg m^{-2} s^{-1})	Comments
Behar et al. [2], 1966	*Flow*/tube	Water, air	–	1	1–1000	NR	ONB influenced by Cg; organic fluids can support a much higher Cg than water
Torikai et al. [3], 1970	Pool/wire	Water, air	0.5–9	0.05–1	NR	–	Shows effect of dissolved gas on pooling boiling superheats; as Cg increases T_s decreases
Murphy and Bergles [4], 1972	*Flow*/tube	R-113, air	0–167	2	1–315	517	Presence of dissolved gas reduces superheat in lower heat flux region
Muller-Steinhagen et al. [5],1986	*Flow*/annulus	Heptane, N_2	NR	1–8	8–400	106–712	Method of pressurization influences heat transfer coefficient; N_2 pressurized heptane shows h enhancement
Muller-Steinhagen et al. [6], 1987	*Flow*/annulus	Water, C_7H_{16}He, N_2, Ar, CO_2, C_3H_8	NR	1–8	0.8–375	202–761	Shows presence of dissolved gases enhances h; at higher q'' curves begin to converge to pure fluid curve
Chao et al. [7], 1994	*Flow*/channel	Water, air	NR	1	17–125	Not reported	Dissolved gasses enhance h; in pseudo-subcooled boiling region enhancement is 20–50%
You et al. [8], 1995	Pool/wire	FC-72, air	17, 214, 480	148–167	1–160	–	Only high Cg enhances h; CHF increases with increasing Cg
Jeschar et al. [9], 1996	Pool/rod	Water, CO_2, O_2	0–619, 0–9	NR	1–2000	–	High Cg stabilize thin film boiling; higher Cg decreases Leidenfrost temperature
O'Connor et al. [10], 1996	Pool/μ-porous surface	FC-72, air	17–1320	1–3	1–500	–	Incipient and nucleate boiling superheats decrease with increase in Cg; suggest two regions on boiling curve—dissolved gas and pure fluid
Hong et al. [11], 1997	Pool/wire	FC-72, air	0–340	NR	1–1000	–	Heater size and Cg effects amount of enhancement; enhancement decreases with increasing q'' and heater size
Adams et al. [12], 1999	*Flow*/channel	Water, air	NR	6–9	500–2500	1998–8352	h is higher for air-saturated than for fully degassed; at higher heat fluxes enhancement is reduced
Adams et al. [13], 1999	*Flow*/channel	Water, air	NR	6	500–2500	1998–8352	Dissolved air increased h by as much as 17%. h enhancement increased w/ increasing q'' and decreasing velocity
Hong et al. [14], 1999	Pool/wire	FC-72, air, He, CO_2	65, 34, 2057	1–116	1–800	–	Dissolved gasses enhance h; same effect with other gasses; as Cg increases CHF increases
Kubo et al. [15], 1999	Pool/reentrant cavities	FC-72, air	17–257	NR	1–190	–	Boiling incipience decreases with increasing Cg

Cui et al. [16], 2000	Pool/droplet	Water, CO_2	1077	1	NR	–	Below T_{sat}—dissolved gas enhances vaporization; dissolved CO_2 suppress heterogeneous bubble formation during impact
Honda et al. [17], 2002	Pool/μ-pin fin	FC-72, air	17–283	NR	1–500	–	Dissolved gas reduced boiling incipience temperature; at high heat fluxes enhancement is decreased
Rainey et al. [18], 2003	Pool/μ-porous flat	FC-72, air	NR	0.3–2	1–800	–	Overall effect of dissolved gas is small; as Cg increases more of nucleate boiling curve is enhanced
Rainey et al. [19], 2003	Pool/μ-porous pin fin	FC-72, air	NR	0.3–2	1–1600	–	Overall effect of dissolved gas is small; as Cg increases more of nucleate boiling curve is enhanced
Steinke and Kandlikar [present work], 2003	*Flow*/μ-channel	Water, air	1.8–8.0	1–2	20–293	375	For details see present paper

[a] As calculated from authors data.

in which a PVC chamber is pressurized using air and a separated membrane. In the second method used for the reduced levels of dissolved air, a pressure cooker is used as the vessel which can be pressurized by heating the water. The degassing procedure used to reduce the dissolved gas content is explained in a later section.

The test section consists of six parallel flow microchannels machined into the copper substrate. Using a microscopic vision system, the channel depth and width are measured at six distinct locations along the channel length. These measurements are used to determine the average dimensions of the channels as: 214 μm width by 200 μm depth and 57.15 mm length. All of the measured values fall within ±5% of the average values. The channels are separated by 600 μm.

The temperature and heat flux in the channels are obtained with two layers of thermocouples located in the copper substrate. The closest thermocouple layer is 3.18 mm from the microchannel wall, and the second layer is 6.35 mm away from the microchannel wall. The first thermocouple is located 6.35 mm from the microchannel inlet in the flow direction. The subsequent thermocouples are located 19.05, 25.4, 38.1, 44.45, and 57.15 mm from the inlet, respectively.

The test section is a combination of three layers and is shown in Fig. 3. The top layer is made of Lexan, an optically clear polycarbonate material. The water inlet and outlet plenums are machined into the polycarbonate layer to eliminate heat transfer in the inlet and outlet manifolds. The second layer is a copper block that is the substrate for the horizontally orientated microchannels. The copper is an electrolytic tough pitch alloy number C11000 with 99.9% copper and 0.04% oxygen (by weight) and a thermal conductivity of 388 W/m K at 20 °C. The third piece is a laminate of epoxy and paper called Phenolic. The Phenolic has a very low thermal conductivity and acts as an insulator on the lower surface of the copper plate. It is also used to secure the microchannel test section with the help of 10 mounting screws. A cartridge heater embedded in the copper section is used to provide the electric input power. All of the outer surfaces are fully insulated with high temperature insulation to minimize heat losses.

The pressure drop for the microchannel was measured between the inlet and exit plenum locations. The pressure drop was used to calculate the friction factor for the microchannels, after accounting for the entrance region, area changes, bends, and exit losses.

Images of nucleation activity are recorded using a high-speed, microscopic image acquisition system. The captured images are used to determine the onset of nucleate boiling. A high-speed, digital CCD camera with a long distance microscope lens was used to gather the images. It is capable of recording at 8000 frames per second. However, the majority of the images are recorded at 1000 fps.

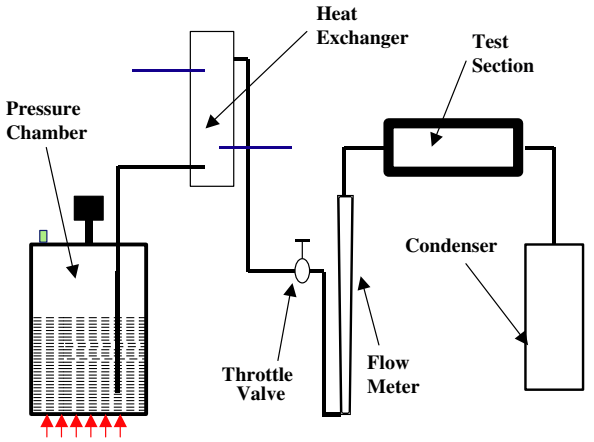

Fig. 2. Fluid delivery system.

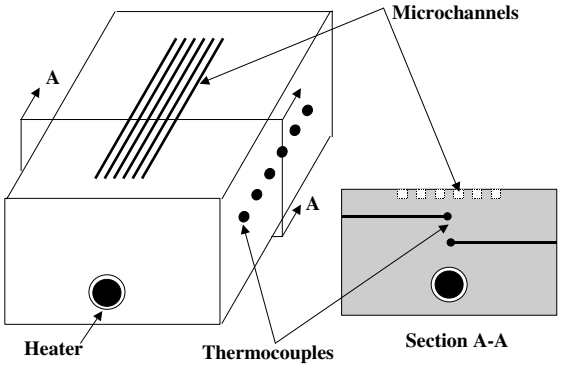

Fig. 3. Microchannel test section.

The uncertainty of the experimental data was determined. The accuracy of the instruments is reported as: $T = \pm 0.1$ °C, $\Delta P = \pm 68.9$ Pa, Volts $= \pm 0.05$ V, $I = 0.005$ A. The bias and precision errors were estimated, and the resulting uncertainty for the heat transfer coefficient is 8.6% at 5 kW/m^2 K and for the friction factor is 7.2% at 0.105.

4. Experimental procedure

The experimental procedures for preparing de-ionized water with different levels of air content are described in this section. There are several different air concentrations used in the present work. As stated previously, the concentration of oxygen in the water will be used as the metric for the dissolved air concentration and will be reported. The concentration of oxygen studied included 8.0, 5.4, and 1.8 ppm.

There are a few steps in preparing water for the gas-saturated water case. The measured oxygen concentration for this case is 8.0 ppm. First, the de-ionized water is filtered and added to the PVC pressure chamber. Secondly, the water in the chamber is isolated from the air used to pressurize the chamber by a membrane. The experiments can begin when the pressure of the water reaches 2 atm absolute pressure.

The procedure for preparing the other concentration cases is described next. First, the same 8 MΩ de-ionized water is added to a pressure chamber. The pressure chamber for these cases is a commercially available pressure cooker equipped with different deadweights for different pressure settings above the atmospheric pressure. Once the desired pressure is attained as the cooker is heated, the deadweight is suddenly removed and the chamber is allowed to blow down and return to atmospheric pressure. A vigorous boiling occurs within the chamber during depressurization. The air dissolved in the water is forced out of the chamber along with the steam. Replacing the deadweight and heating once again pressurizes the cooker to provide flow. The 0.3 atm deadweight and one blown down yielded an oxygen concentration of 5.4 ppm. The 1 atm deadweight and two blown downs yielded an oxygen concentration of 1.8 ppm.

Two different deadweights corresponding to 0.34 and 1 atm are used on the pressure cooker while it is heated to supply pressurized water to the test section. After the above degassing procedure, the water is degassed to a saturation temperature of 108 and 121 °C, respectively. The remaining dissolved air will not desorb from the water as long as the heater surfaces stays below the respective degassing temperatures. Steam continually escapes from the chamber when the deadweight is again applied. This step ensures that air does not enter the chamber and come into contact with the water.

Initially, a series of experiments are performed to establish the heat loss characteristics of the test section. The water is completely removed from the test section during these runs. Power is applied and the test section is allowed to reach a steady state. The heat loss is plotted against the temperature difference between the test section and the ambient air. The slope of this plot is used to determine the lost power for a given test section operating temperature.

The experiment can begin once the water is prepared as previously described. In both cases, water is drawn from the bottom of the pressure vessel and passes through a flat plate heat exchanger to adjust the water inlet temperature to the test section. A variable area flow meter is used to measure the flow rate. LabVIEW is used to monitor the thermocouples measuring temperature. The flow is started in the channel and the cartridge heater is powered. The mass flow rate is held constant while the input power is varied through the desired range. The resulting thermal performance was recorded in terms of water flow rate, inlet and outlet water temperatures, 12 temperatures inside the copper block and the inlet and exit pressures.

The images are acquired after the system has reached steady state to detect nucleation in the flow channel. A microscopic lens with lower magnification is used view all six channels. This was used to determine channel interactions and to locate nucleation sites. Once the entire channel is imaged, the microscopic lens with higher resolution is used to gather detailed images of specific features and events.

5. Data analysis

The method of analysis for the data obtained during the experiments is described in this section. The surface temperature is determined using the two rows of embedded thermocouples that are located at different depths from the microchannel surface. The surface temperatures are calculated using the heat flux value obtained from the thermocouple measurements. The log mean temperature difference method was used to calculate the average heat transfer coefficient as given by Eq. (3). The average heat transfer coefficient is found using Eq. (4).

$$\Delta T_{\mathrm{LMTD}} = \frac{(T_{\mathrm{s}} - T_{\mathrm{i}}) - (T_{\mathrm{s}} - T_{\mathrm{o}})}{\ln\left(\frac{T_{\mathrm{s}} - T_{\mathrm{i}}}{T_{\mathrm{s}} - T_{\mathrm{o}}}\right)} \tag{3}$$

$$\bar{h} = \frac{q_{\mathrm{TS}}}{A * \Delta T_{\mathrm{LMTD}}} \tag{4}$$

The present microchannels are heated from three sides. The thermal conductivity of the Lexan cover plate is very small compared to the copper substrate. The amount of heat that flows through the cover plate is negligible. Therefore, the Lexan cover plate can be considered to be adiabatic.

The heat transfer surface area used for the calculation is found using the channel dimensions measurements described earlier. The average Nusselt number is calculated from Eq. (5).

$$\overline{Nu} = \frac{\bar{h} D_{\mathrm{h}}}{k_{\mathrm{f}}} \tag{5}$$

The theoretical value of the Nusselt number for the case of constant wall temperature and for constant heat flux is given by Eqs. (6) and (7), respectively [21].

$$Nu_{\mathrm{T}} = 7.541(1 - 2.61\alpha^* + 4.97\alpha^{*^2} - 5.119\alpha^{*^3} + 2.702\alpha^{*^4} - 0.548\alpha^{*^5}) \tag{6}$$

$$Nu_{\mathrm{H}} = 8.235(1 - 2.0421\alpha^* + 3.0853\alpha^{*^2} - 2.4765\alpha^{*^3} + 1.0578\alpha^{*^4} - 0.1861\alpha^{*^5}) \tag{7}$$

where α^* is the aspect ratio. Based upon the present geometry, the values of Nu_{T} and Nu_{H} are 2.969 and 3.616 respectively. The variation of the fluid properties due to the variation in the temperature cause some variation in predicted Nusselt numbers. The Nusselt Number is corrected for temperature dependent properties using Eq. (8) [21].

$$\frac{Nu}{Nu_{\mathrm{cp}}} = \left(\frac{\mu_{\mathrm{w}}}{\mu_{\mathrm{m}}}\right)^n \tag{8}$$

where, Nu is the corrected Nusselt number, Nu_{cp} is the constant property solution, μ_{w} is the viscosity of the fluid at the wall temperature, and μ_{m} is the viscosity of the fluid at the mean temperature. The exponent n is equal to -0.14 for a laminar, fully developed, and heating flow. The experimental value of the average constant property Nusselt number was around 2.0. There are a few reasons for the discrepancy. The heat transfer coefficients based upon the log mean temperature difference is used in the Nusselt number calculations. Unfortunately, the difference in temperature between the outlet water temperature and the surface temperature is on the order of 0.1 °C. This very small ΔT is on the same order of magnitude as the experimental uncertainty. Therefore, the Nusselt numbers cannot be reliably calculated. This highlights the difficulty in obtaining accurate single-phase heat transfer data in highly efficient microchannels. In addition, the test section was heated from the three sides, while the predicted value from Eq. (5) corresponds to uniform temperature on all four sides.

The overall pressure drop is adjusted for entrance and exit losses to determine the frictional pressure drop in the microchannels. There are losses due to the contraction from the larger inlet plenum into the

microchannels and the expansion from the microchannels into the larger exit plenum. The Fanning friction factor for laminar flow is determined from the correlation from Shah and London [21] and is given in Eq. (9).

$$f\,Re = 24(1 - 1.3553\alpha^* + 1.9467\alpha^{*2} - 1.7012\alpha^{*3} + 0.9564\alpha^{*4} - 0.2537\alpha^{*5}) \quad (9)$$

For the microchannel geometry, the fRe product is found to be 14.25. For liquids in laminar flow, a common methodology is to apply the viscosity correction factor as given Eq. (10)

$$\frac{f}{f_{cp}} = \left(\frac{\mu_w}{\mu_m}\right)^{0.58} \quad (10)$$

There is no experimental study available confirming the above relationship for single-phase flow in microchannels. Since these are empirically derived relations, they need to be verified for microchannels, although they are expected to be valid as no additional mechanisms of heat or momentum transfer are introduced. Specifically, the effect of temperature on the friction factor described by Eq. (10) needs to be validated. Also, the Nusselt number is expected to be somewhat different for the present case of three sided heating in the microchannel.

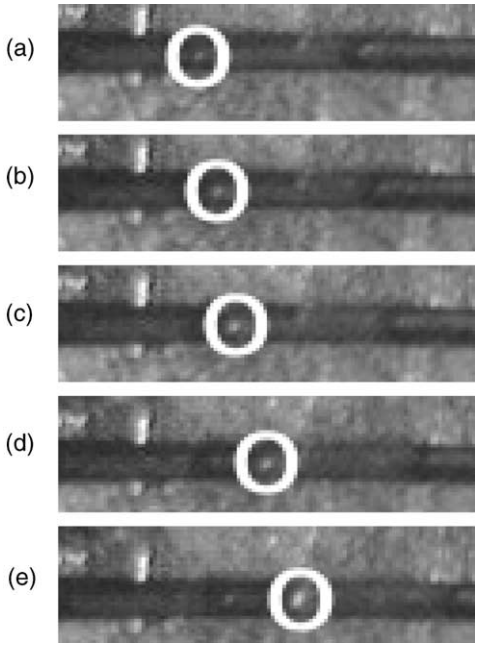

Fig. 4. Nucleation and bubble growth in microchannel. Flow is from left to right, single channel shown. Bubble diameter: (a) 67 μm and (e) 160 μm. For: $G = 347$ kg/m^2 s, $q''_{ts} = 41.7$ kW/m^2, $x = 0.002$, $\Delta t = 1$ ms, $C = 1.8$ ppm.

6. Results

Experiments are performed to obtain the effect of dissolved gas on heat transfer and pressure drop for microchannel flows. The mass flux is held constant and the heat flux was varied for each data set. The flow is in the laminar range with a Reynolds number of 150, calculated based upon inlet saturation conditions for all-liquid flow. The heat flux ranged from 20 to 293 kW/m^2.

The flow visualization system was used to determine the incipience of boiling in the microchannels. The vision system was also used to ensure that the flow distribution in each of the microchannels is similar. The nucleation and flow of bubbles was observed and measured to ensure a reasonably uniform distribution of flow in the microchannels. Fig. 4 shows the nucleation and growth of a bubble in the microchannel. A single channel is shown and the flow is from left to right. The bubble nucleates in the channel in the first frame (Fig. 4a). The second frame shows the bubble beginning to grow. As the bubble grows it begins to slide along the surface of the microchannel (Fig. 4(b)–(d)). Finally, the bubble reaches departure diameter and moves in the bulk flow.

A plot of heat flux vs. the wall temperature near the exit of the channel is shown in Fig. 5. The transition from the single-phase to two-phase is seen as a marked change in slope. Nucleation occurs at a lower surface temperature than the saturation temperature. Following early nucleation, a reduction in heat flux is seen for the 8.0 ppm case. Nucleation was detected at a surface temperature of 90.5 °C. The desorption of the dissolved air forms bubbles of air and a limited amount of water vapor to form on the nucleation sites. As a result, the nucleation site becomes active at a surface temperature below that of the saturation temperature.

Fig. 6 shows the average heat transfer coefficient vs. heat flux for the three different levels of dissolved air. The heat transfer coefficient of the 8.0 ppm case first decreases before the saturation temperature and then increases above the 5.4 and 1.8 ppm cases beyond the saturation temperature. Such a decrease was not reported by earlier investigators for large diameter channels, but is consistently observed in the present work. The effect of gas content is seen in the 8.0 ppm case by a reduction in heat transfer coefficient, as nucleation occurs. The boiling incipience occurs at a surface temperature of 90.5 °C for the 8.0 ppm case. The dissolved air is now coming out of water at this point and forms an insulating layer of bubbles containing air–water vapor mixture. This layer is believed to be responsible for the decrease in heat transfer coefficient observed in Fig. 6. As the surface temperature of the channel approaches the saturation temperature, the 8.0 ppm case heat transfer coefficient increases above the degassed cases. Beyond a certain heat flux and surface temperature, fully

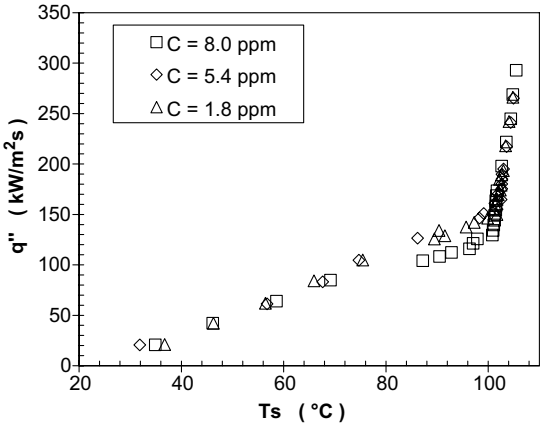

Fig. 5. Heat flux vs. exit surface temperature. For: $C = 8.0$, 5.4, and 1.8 ppm; $G = 380$ kg/m^2 s; $2.0\times10^4 < q'' < 3.5\times10^5$ W/m^2, $-0.1 < x < 0.1$.

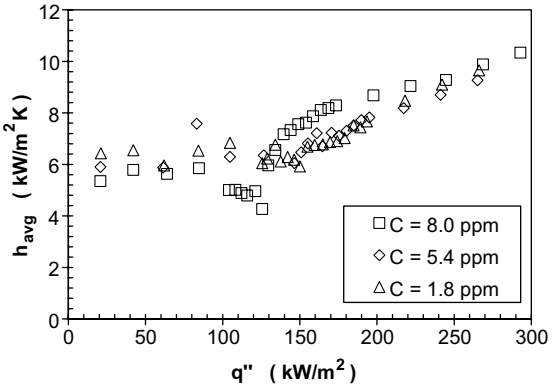

Fig. 6. Heat transfer coefficient vs. heat flux. For: $C = 8.0$, 5.4, and 1.8 ppm; $G = 380$ kg/m^2 s; $2.0\times10^4 < q'' < 3.5\times10^5$ W/m^2, $-0.1 < x < 0.1$.

developed boiling ensues and all of the heat transfer coefficients for different dissolved gas cases collapse on a single curve. This behavior is in agreement with previous investigators results.

The heat loss for each data point is determined from the calibration tests conducted prior to tests. The actual heat transferred into the test section is used in determining the exit quality. The heat transfer coefficient vs. exit quality is shown in Fig. 7. The exit quality ranges from −0.12 to 0.12. Table 2 presents the observed nucleation surface temperature for each of the oxygen concentration levels. It shows that for the reduced levels of dissolved air, the incipience of boiling occurs very close to the saturation temperature. However, the high concentration level of 8.0 ppm has the boiling incipience at 90.5 °C. The reduction in boiling incipience temperature is consistent with previous works.

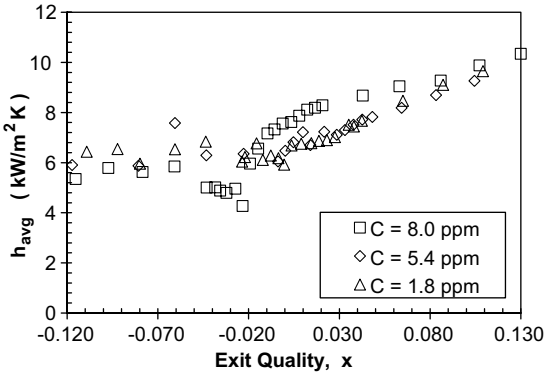

Fig. 7. Heat transfer coefficient vs. exit quality. For: $C = 8.0$, 5.4, and 1.8 ppm; $G = 380$ kg/m^2 s; $2.0\times10^4 < q'' < 3.5\times10^5$ W/m^2, $-0.1 < x < 0.1$.

Table 2
Observed surface temperatures for different levels of dissolved air

O_2 concentration (ppm)	T_w (°C)
1.8	99.9
5.4	99.7
8.0	90.5

The adiabatic friction factor for laminar flow is first determined experimentally to provide validity of the test section and measurement techniques. The adiabatic friction factor for the microchannel is shown in Fig. 8. The adiabatic friction factor is in good agreement with the predicted friction factor. The experimental data is generally within 10% of the predicted value.

The diabatic pressure drop was measured during all of the heat transfer experiments. The measured pressure was taken across the length of the microchannel as the fluid entered and exited the microchannel. The diabatic friction factor is further corrected using Eq. (10) to obtain the constant property friction factors, as shown in Fig. 9. Only the all-liquid, single-phase flow friction factors are correlated. The increasing friction factors seen on the right side of the graph are due to two-phase flow.

The experimentally determined f values using the property correction factor for single-phase flow under diabatic condition are in good agreement with the predicted values prior to nucleation. With the onset of nucleation, the friction factors are seen to increase. This behavior was found consistently in all experiments. The presence of a bubble boundary layer attached to the wall is believed to cause this effect for the 8.0 ppm case. The two-phase flow shows an increase in f, as expected, above the single-phase values. The two-phase friction

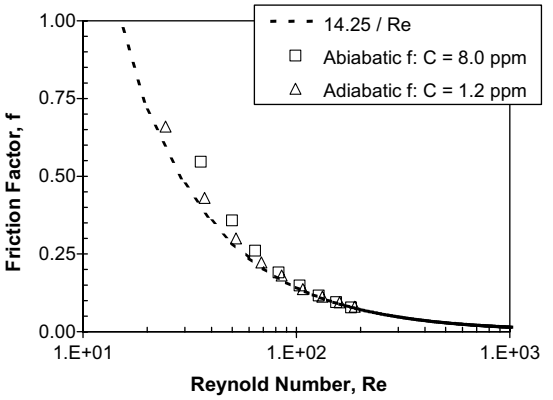

Fig. 8. Adiabatic friction factor vs. Reynolds number. For: $C = 8.0$ and 1.8 ppm; $G = 380$ kg/m^2 s; $q'' = 0.0$ W/m^2.

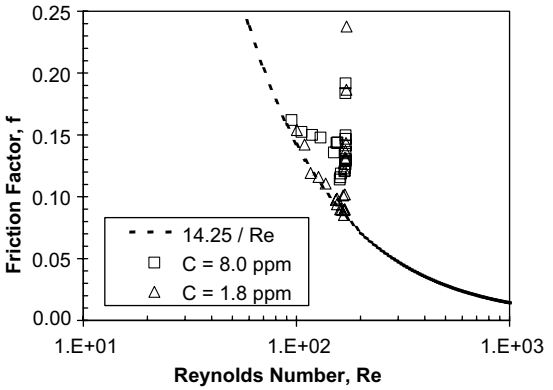

Fig. 9. Diabatic friction factor vs. Reynolds number. For: $C = 8.0$, 5.4, and 1.8 ppm; $G = 380$ kg/m^2 s; $2.0\times10^4 < q'' < 3.5\times10^5$ W/m^2, $-0.1 < x < 0.1$.

factor is not correlated because of the small number of data points in this region.

7. Conclusions

An experimental investigation is conducted to study the effect of dissolved gas on nucleation heat transfer and pressure drop during flow boiling of water in microchannels. The heat transfer characteristics are investigated for three levels of dissolved air content in the water. The adiabatic and diabatic friction factors for laminar flow in 207 μm hydraulic diameter, parallel microchannels are studied as a function of dissolved gas content. The following conclusions are drawn from the present study.

1. An apparatus and procedure to deliver de-ionized water with controlled levels of dissolved air has been developed. The unit is able to deliver water with controlled amounts of dissolved gases in the range of 1.8–8.0 ppm of dissolved oxygen content.
2. The boiling incipience surface temperatures varied for the three different levels of dissolved air. The dissolved air concentrations for the 1.8 and 5.4 ppm cases begins nucleation at a surface temperature very close to saturation temperature at 1 atm. However, the 8.0 ppm case has nucleation beginning at a surface temperature of 90.5 °C. This result agrees with previous investigators works.
3. There is a slight decrease in heat transfer coefficient for the 8.0 ppm case after the boiling incipience wall temperatures are achieved. The desorption of the dissolved air is believed to form an insulating layer of bubbles on the heater surface. This result was not reported by previous investigators in large diameter channels. When the surface temperature reaches the local liquid saturation temperature, the heat transfer coefficient experiences an enhancement over the 5.4 and 1.8 ppm cases. At higher heat fluxes, all three cases collapse on the same curve. This result also agrees with the observations of previous investigators.
4. The adiabatic single-phase friction factor for laminar flow of water in microchannels is accurately described by the established relationship for large (conventional) diameter channels. The diabatic friction factors can be accurately predicted using the property ratio correction factors used for large diameter (conventional) channels.

Acknowledgements

All of the work was conducted in the Thermal Analysis and Microfluidics Laboratory at RIT. The authors would also like to thank RIT students Christopher Fullone and Prabhu Balasubramanian for their assistance in the design and data collection during the course of this work. The support provided by Rochester Institute of Technology is gratefully acknowledged.

References

[1] J.A. Dean, Lange's Handbook of Chemistry, McGraw-Hill, New York, 1992.
[2] M. Behar, M. Courtaud, R. Ricque, R. Semeria, Fundamental aspects of subcooled boiling with and without dissolved gases, Proc. Int. Heat Transfer Conf. 4 (1966) 1–11.
[3] K. Torikai, H. Shimamune, T. Fujishiro, The effect of the dissolved gas content upon incipient boiling superheats, in: Proceedings of the 4th International Heat Transfer Conference, Paris and Versailles, France B 2.11, Elseveir Publications, 1970.

[4] R.C. Murphy, A.E. Bergles, Subcooled flow boiling of fluorocarbons—hysteresis and dissolved gas effects on heat transfer, in: Proceedings of Heat Transfer and Fluid Mechanics Inst, Stanford University Press, 1972, pp. 400–416.
[5] H. Muller-Steinhagen, A.P. Watkinson, N. Epstein, Subcooled-boiling and convective heat transfer to heptane flowing inside an annulus and past a coiled wire: Part I—experimental results, J. Heat Transfer 108 (1986) 922–927.
[6] H. Muller-Steinhagen, N. Epstein, A.P. Watkinson, Effect of dissolved gases on subcooled flow boiling heat transfer, Chem. Eng. Process. 23 (2) (1988) 115–124.
[7] W.-W. Chao, J.F. Kunze, W. Dai, S.K. Loyalka, Effect of dissolved gas bubble nucleation on natural convection heat transfer in narrow channels, Nucl. Technol. 105 (2) (1994) 261–270.
[8] S.M. You, T.W. Simon, A. Bar-Cohen, Y.S. Hong, Effects of dissolved-gas content on pool boiling of a highly wetting fluid, J. Heat Transfer 117 (1995) 687–692.
[9] R. Jeschar, H. Kraushaar, H. Griebel, Influence of gases dissolved in cooling water on heat transfer during stable film boiling, Steel Res. 67 (6) (1996) 227–234.
[10] J.P. O'Connor, S.M. You, J.Y. Chang, Gas-saturated pool boiling heat transfer from smooth and micro porous surfaces in FC-72, J. Heat Transfer 118 (1996) 662–667.
[11] Y.S. Hong, C.N. Ammerman, S.M. You, Boiling characteristics of cylindrical heaters in saturated, gas saturated, and pure-subcooled FC-72, J. Heat Transfer 119 (1997) 313–318.
[12] T.M. Adams, S.M. Ghiaasiaan, S.I. Abdel-Khalik, Enhancement of liquid forced convection heat transfer in microchannels due to the release of dissolved noncondensables, Int. J. Heat Mass Transfer 42 (1999) 3563–3573.
[13] T.M. Adams, S.M. Ghiaasiaan, S.I. Abdel-Khalik, Enhancement of liquid forced convection heat transfer in microchannels due to the release of dissolved noncondensables, in: Proceedings of National Heat Transfer Conference, August 15–17, 1999, Albuquerque, New Mexico, Paper# 263, ASME Publications, 1999.
[14] Y.S. Hong, C.N. Ammerman, S.M. You, Investigation of local degassing effects on heat transfer during gas-saturated boiling from a small cylinder, Am. Soc. Mech. Eng., Heat Transfer Div. HTD 364-2 (1999) 51–59.
[15] H. Kubo, H. Takamatsu, H. Honda, Effects of size and number density of micro-reentrant cavities on boiling heat transfer from a silicon chip immersed in degassed and gas-dissolved FC-72, J. Enhanced Heat Transfer 6 (2–4) (1999) 151–160.
[16] Q. Cui, S. Chandra, S. McCahan, Enhanced boiling of water droplets containing dissolved gases or solids, in: Proceedings of 34th National Heat Transfer Conference, Pittsburgh, PA, Paper No. NHTC2000-12249, 2000, pp. 1–12.
[17] H. Honda, H. Takamastu, J.J. Wei, Enhanced boiling of FC-72 on silicon chips with micro-pin-fins and submicron-scale roughness, J. Heat Transfer 124 (2002) 383–390.
[18] K.N. Rainey, S.M. You, S. Lee, Effect of pressure, subcooling, and dissolved gas on pool boiling heat transfer from microporous surfaces in FC-72, J. Heat Transfer 125 (2003) 75–83.
[19] K.N. Rainey, S.M. You, S. Lee, Effect of pressure, subcooling, and dissolved gas on pool boiling heat transfer from microporous, square pin-finned surfaces in FC-72, Int. J. Heat Mass Transfer 46 (2003) 23–35.
[20] S.G. Kandlikar, W.J. Grande, Evolution of microchannel flow passages—thermohydraulic performance and fabrication technology, in: Proceedings of International Mechanical Engineering Congress and Exposition, November 17–22, 2002, New Orleans, LA. Paper # IMECE02-32043, ASME Publications.
[21] R.K. Shah, A.L. London, Laminar Flow Forced Convection in Ducts Supplement 1 to Advances in Heat Transfer, Academic, New York, 1978.